

1 **Quantification of gallium cryo-FIB milling damage in biological lamella**

2 Bronwyn A. Lucas^{a*} and Nikolaus Grigorieff^{a,b*}

3
4 ^a RNA Therapeutics Institute, and ^b Howard Hughes Medical Institute, University of
5 Massachusetts Chan Medical School, Worcester, MA

6 7 8 ***Correspondence:**

9 Bronwyn A. Lucas, bronwyn.lucas@umassmed.edu, ORCID: 0000-0001-9162-0421

10 Nikolaus Grigorieff, niko@grigorieff.org, ORCID: 0000-0002-1506-909X

11 12 **Author Contributions:**

13 BAL conceived the project, designed the experiments, performed the wet-bench experiments,
14 collected the cryo-EM data, wrote data analysis code, interpreted the data, wrote the manuscript,
15 and contributed to acquisition of funding. NG acquired funding and contributed to experimental
16 design, interpretation of results, and review and editing of the manuscript.

17
18 **Competing Interest Statement:** The authors declare no conflict of interest.

19
20 **Classification:** Biophysics, structural biology

21
22 **Keywords:** Electron cryo-microscopy, template matching, ribosome, focused ion beam milling

23 24 **This PDF file includes:**

25 Main Text

26 Figures 1 to 4

27 Supplementary Figures 1 to 6

28 Supplementary Table 1

29 **Significance:**

30 The molecular mechanisms of biological macromolecules and their assemblies is often studied
31 using purified material. However, the composition, conformation and function of most
32 macromolecules depend on their cellular context, and therefore, must also be studied inside cells.
33 Focused ion beam (FIB) milling enables cryogenic electron microscopy to visualize
34 macromolecules in cells at close to atomic resolution by generating thin sections of frozen cells.
35 However, the extent of FIB-milling damage to frozen cells is unknown. Here we show that Ga^+
36 FIB-milling introduces damage to a depth of ~60 nm from each lamella surface, leading to a loss
37 of recoverable information of up to 20% in 100 nm samples. FIB-milling with Ga^+ therefore
38 presents both an opportunity and an obstacle for structural cell biology.

39

40

41

42

43

44

45

46

47

48

49

50

51

52

53

54

55 **Abstract:**

56 Cryogenic electron microscopy (cryo-EM) has the potential to reveal the molecular details of
57 biological processes in their native, cellular environment at atomic resolution. However, few
58 cells are sufficiently thin to permit imaging with cryo-EM. Thinning of frozen cells to <500 nm
59 lamellae by cryogenic focused ion beam (FIB) milling has enabled visualization of cellular
60 structures with cryo-EM. FIB-milling represents a significant advance over prior approaches
61 because of its ease of use, scalability, and lack of large-scale sample distortions. However, the
62 amount of damage caused by FIB-milling to the generated thin cell section has not yet been
63 determined. We recently described a new approach for detecting and identifying single
64 molecules in cryo-EM images of cells using 2D template matching (2DTM). 2DTM is sensitive
65 to small differences between a molecular model (template) and the detected structure (target).
66 Here we use 2DTM to demonstrate that under the standard conditions used for machining
67 lamellae of biological samples, FIB-milling introduces a layer of variable damage that extends to
68 a depth of 60 nm from each lamella surface. This thickness exceeds previous estimates and limits
69 the recovery of information for *in situ* structural biology. We find that the mechanism of FIB-
70 milling damage is distinct from radiation damage during cryo-EM imaging. By accounting for
71 both electron scattering and FIB-milling damage, we find that FIB-milling damage will negate
72 the potential improvements from lamella thinning beyond 90 nm.

73

74

75 **Main text**

76

77 **Introduction**

78 Cryogenic electron microscopy (cryo-EM) has enabled visualization of purified
79 macromolecular complexes at atomic resolution (1, 2). A more complete understanding of
80 molecular function requires visualizing their location, structure, and interactions in the native
81 cellular environment. The internal architecture of cells can be preserved with high fidelity by
82 vitrification allowing for the visualization of molecules at high resolution directly in the cell (*in*
83 *situ*) with cryo-EM (1). However, with few exceptions, cells are too thick to be electron-
84 transparent, and therefore require thinning.

85 Cryo-EM of vitreous sections (CEMOVIS) was an initial solution to generating thin
86 slices of high-pressure frozen cells using a cryo-ultramicrotome (2). However, the process
87 requires a skilled user, is difficult to automate and introduces compression artifacts, which
88 together have limited the widespread utility of this approach (3).

89 Focused ion beam (FIB) milling is a technique in common use in materials science that
90 has been adapted to produce thin cell sections for *in situ* cryo-EM under cryogenic conditions
91 (4–6). In place of a physical ultramicrotome, a focused beam of ions, typically produced from a
92 gallium liquid metal ion source (LMIS), is used to sputter material above and below a thin
93 section of the cell known as a lamella (6). FIB-milling has higher throughput relative to
94 CEMOVIS because of its ease of use, commercial availability, and computational control
95 allowing for automation of lamella production (7, 8). As a result, cryo-FIB milling for TEM
96 lamella preparation of cells has recently seen widespread adoption and is now the predominant
97 method for preparing cells for *in situ* cryo-EM (9).

98 It has been demonstrated recently that it is possible to generate near-atomic resolution
99 reconstructions by averaging subtomograms from vitreously frozen cells (10, 11). These
100 successes highlight the need for a more quantitative understanding of potential sample damage
101 introduced during FIB-milling that could limit both the resolution of *in situ* reconstructions and
102 the ability to accurately localize molecules in cells.

103 Organic materials are particularly sensitive to radiation damage upon interaction with
104 high-energy particles. Simulations of the stopping range in matter (SRIM) of ions in a glancing
105 incidence beam at 30 keV, the typical conditions for cryo-lamella preparation for TEM, will

106 implant Ga⁺ ions in frozen cells to a depth of 20-30 nm (5, 12). After accounting for removal of
107 ~10 nm of material due to the concurrent milling action, the implantation zone is anticipated to
108 be ~10-20 nm from the lamella surface (5). Cascading atomic collisions between Ga⁺ ions and
109 sample atoms as the Ga⁺ ions imbed in the sample will introduce additional damage to an
110 unknown depth from each lamella surface (13). Such damage introduced during FIB-milling
111 would decrease the usable volume of a lamella and could limit the resolution of *in situ*
112 determined structures. Cryo-electron tomography (cryo-ET), the predominate method for
113 characterizing molecular structure *in situ*, generates tomograms that are limited in resolution to
114 about 20 Å (14), and is therefore not suitable for measuring differences in individual particle
115 quality at high-resolution.

116 We have recently described a new approach, 2D template matching (2DTM) (15), to
117 locate molecular assemblies in three dimensions with high precision in 2D cryo-EM images of
118 unmilled cells (16, 17) and FIB-milled lamellae (18). Cross-correlation of a high-resolution
119 template generated from a molecular model with a cryo-EM image produces a 2DTM signal-to-
120 noise ratio (SNR) that reflects the similarity between the template and the individual target
121 molecules in the image (15–18).

122 In the present study, we apply 2DTM to quantify target integrity within FIB-milled
123 lamellae at single molecule resolution. We find that FIB-milling appreciably reduces target
124 integrity to a depth of ~60 nm from the lamella surface, more than previously appreciated. We
125 find that the nature of FIB-milling damage is distinct from electron radiation damage, consistent
126 with inter-atomic collisions, rather than electronic interactions, being responsible for the damage.
127 By comparing signal loss due to FIB-milling damage to signal loss in thick samples due to
128 inelastic electron scattering and molecular overlap, we show that recovery of structural
129 information in 100 nm lamellae is reduced by ~20%.

130

131 **Results**

132 ***FIB-milling introduces a layer of reduced structural integrity***

133 A 2DTM template represents an ideal, undamaged model of the molecule to be detected. Any
134 damage introduced during FIB-milling will therefore decrease the correlation with the
135 undamaged template, leading to a lower 2DTM SNR. Ribosomes are present at high density and
136 relatively evenly distributed in the cytoplasm of the yeast *Saccharomyces cerevisiae* (18), and

137 therefore present an ideal 2DTM target to quantify differences in target integrity. We prepared
138 FIB-milled lamellae of *S. cerevisiae* cells of thickness varying from 120 nm to 260 nm (**Fig. 1A**
139 **and B**). In 30 images of the yeast cytoplasm from four lamellae, we located 11030 large
140 ribosomal subunits (LSUs) using 2DTM (**Fig. 1C and D, SI Appendix, Fig. S1A and B**).

141 We estimated the z-coordinate of each LSU relative to the image defocus plane with 2 nm
142 precision (**Fig. 1E and F**, see Methods). We found that the LSUs were located in a slab oriented
143 at an angle of $\sim 6\text{--}11^\circ$ relative to the defocus plane, consistent with the milling angle relative to
144 the grid surface (**Fig. 1C-F**). The 2DTM SNRs of LSUs were noticeably lower at the edge of the
145 lamellae than at the center and did not correlate with defocus (**Fig. 1E and F**), indicating that
146 this is unlikely to be the result of defocus estimation error. We used the tilt axis and angle
147 estimated from the contrast transfer function (CTF) fit (18, 19) to adjust the coordinate frame to
148 reflect the position of each LSU relative to the lamella center (**Fig. 1G and H**).

149 On average, the 2DTM SNRs were higher in the center and lower towards the surface in all
150 lamellae examined (**Fig. 1G and H, SI Appendix, Fig. S2**). The maximum 2DTM SNR
151 decreased with increasing lamella thickness (**SI Appendix, Fig. S1B**) as observed previously
152 (15–18). However, we observed a different 2DTM SNR profile as a function of z-coordinate in
153 regions of different thicknesses. The 2DTM SNRs in $\leq \sim 150$ nm thick lamellae increased
154 towards the center of the lamella (e.g.: **Fig. 1G**), while in $\geq \sim 150$ nm thick lamellae they
155 reached a plateau (e.g.: **Fig. 1H**). This is consistent with decreased structural integrity of LSUs
156 close to each lamella surface.

157

158 *Quantification of the damage profile reveals damage up to ~ 60 nm from each lamella surface*

159 To assess the depth of the damage we focused on images of 200 nm lamellae because we
160 were able to detect targets throughout most of the volume, and both the number and 2DTM
161 SNRs reached a plateau in the center, indicating that there is zone of minimal damage. In seven
162 images of 200 nm lamellae, we calculated the mean 2DTM SNR in bins of 10 nm from the
163 lamella surface and divided this by the undamaged SNR (SNR_u), defined as the mean 2DTM
164 SNR of the targets between 90 and 100 nm from the lamella surface. Both the relative 2DTM
165 SNR (**Fig. 2A**) and the number of LSUs detected (**Fig. 2B**) increased as a function of distance
166 from the lamella surface. The lower number of detected LSUs at the lamella surface is likely a
167 consequence of targets having a 2DTM SNR that falls below the chosen 2DTM SNR threshold

168 of 7.85 at which we expect a single false positive per image (15). Consistently, in each of the
169 bins >60 nm from the lamella surface (**Fig. 2C**), the distribution of 2DTM SNRs was Gaussian
170 and not significantly different from the undamaged bin (t-test $P > 0.05$, **SI Appendix Table S1**).
171 However, for each of the bins ≤ 60 nm from the lamella surface, the distribution shifts
172 significantly (t-test $P < 0.0001$, **SI Appendix Table S1**) to the left, i.e., lower SNR values (**Fig.**
173 **2C**). This indicates that the structural similarity between target and template decreases closer to
174 the lamella surface. We interpret this as a loss of target integrity due to FIB-milling damage up to
175 ~ 60 nm from the lamella surface.

176 We found that the change in the mean 2DTM SNR at a particular depth relative to the
177 lamella surface (d) relative to SNR_u can be described by an exponential decay function:

$$178 \quad \quad \quad 179 \quad \quad \quad SNR_d/SNR_u = 1 - Y_0 \cdot e^{-\frac{d}{k}} \quad (1)$$

180
181 where Y_0 is the relative damage at the lamella surface and k is the damage constant. A least-
182 squares fit gave values of $Y_0 = 0.31$ and $k = 37.03$ nm ($R^2 = 0.99$) (**Fig. 2D**). Since SNR_d/SNR_u
183 represents the remaining signal the exponential model indicates a steep decline in damage in the
184 first ~ 10 - 20 nm from the lamella surface, possibly explaining why few LSUs were detected in
185 this range.

186 The observed damage profile was absent in images of unmilled *Mycoplasma pneumoniae*
187 cells, confirming that the observed pattern results from FIB-milling and is not a result of error in
188 the z-estimation in 2DTM (**SI Appendix, Fig. S4 and 5**).

189 190 **Mechanism of FIB-milling damage**

191 To characterize the mechanism of FIB-milling damage we compared its profile to the
192 damage introduced by exposure to electrons during cryo-EM imaging. Cryo-EM imaging causes
193 radiation damage, introducing differences between the template and the target structure that are
194 more pronounced at high spatial frequencies (20). To measure radiation damage, we generated a
195 series of low-pass filtered templates with a sharp cut-off at different spatial frequencies and
196 calculated the change in the 2DTM SNR of each identified large ribosomal subunit as a function
197 of electron exposure relative to exposure to 20 electrons/ \AA^2 (**Fig. 3A and B**). We find that the
198 2DTM SNR of templates low-pass filtered to between $1/10$ and $1/7 \text{\AA}^{-1}$ increases with increasing

199 exposure. The 2DTM SNRs of templates low-pass filtered with a cut-off at higher resolutions
200 begin to decrease with increasing exposure (**Fig. 3A and B**). Templates filtered to $1/5 \text{ \AA}^{-1}$ have a
201 maximum 2DTM SNR at 32 electrons/ \AA^2 while templates filtered to $1/3 \text{ \AA}^{-1}$ have a maximum
202 2DTM SNR at 28 electrons/ \AA^2 (**Fig. 3B**).

203 To estimate the extent of FIB-milling damage on different spatial frequencies we binned
204 detected targets by lamella depth and calculated SNR_d/SNR_u . We found that for templates
205 filtered to $< 1/5 \text{ \AA}^{-1}$, SNR_d/SNR_u fluctuated for targets detected further from the lamella center.
206 This is likely due to differences in the defocus position that result in some of the targets having
207 weak contrast (CTF close to zero) and therefore not contributing meaningful signal at different
208 spatial frequencies relative to targets in the center of the lamella. For templates filtered to $> 1/5$
209 \AA^{-1} the profile was similar between the different bins and approximately constant across spatial
210 frequencies (**Fig. 3C and D**). This is consistent with a model in which the FIB-damaged targets
211 have effectively lost a fraction of their structure, compared to undamaged targets, possibly due to
212 displacement of a subset of atoms by colliding ions.

213 Radiation damage of nucleic acids has been well documented with one of the most labile
214 bonds being the phosphodiester bond in the nucleic acid backbone (21) (**Fig. 3E**). We observed
215 an accelerated loss of signal from phosphorous atoms relative to the average loss of signal for the
216 whole template as a function of electron exposure (**Fig. 3F**). This is consistent with the
217 phosphorous atoms being more mobile due to breakage of phosphodiester linkages in response to
218 electron exposure. We did not observe a consistent difference in the accelerated loss of signal
219 from phosphorous in the lamella z-coordinate groups (**Fig. 3F**). This indicates that the
220 mechanism for FIB-milling damage is distinct from the radiation damage observed during cryo-
221 EM imaging.

222

223 *Sample thickness limits 2DTM SNR more than FIB-milling damage*

224 Above we report that using the most common protocol for cryo-lamella generation by LMIS
225 Ga^+ FIB-milling introduces a variable layer of damage up to 60 nm from each lamella surface.
226 Lamellae for cryo-EM and cryo-ET are typically milled to 100-300 nm, meaning that the
227 damaged layer comprises 50-100% of the volume. Thicker lamellae will have a lower proportion
228 of damaged particles. However, thicker lamellae will also suffer from signal loss due to the
229 increased loss of electrons due to inelastic scattering and scattering outside the aperture, as well

230 as the increased number of other molecules in the sample contributing to the background in the
231 images. For a target inside a cell, the loss of 2DTM SNR with increasing thickness has been
232 estimated as (16):

$$233$$
$$234 \quad SNR_t/SNR_0 = e^{-t/\lambda_{SNR}} \quad (2)$$
$$235$$

236 where t denotes the sample thickness, SNR_0 is the 2DTM SNR in the limit of an infinitesimally
237 thin sample, and the decay constant $\lambda_{SNR} = 426$ nm. Optimal milling conditions for high
238 resolution imaging of FIB-milled lamellae will therefore need to strike a balance between
239 lamella thickness and FIB damage.

240 To assess the relative impact of these two factors on target detection with 2DTM we
241 plotted the proportional loss in signal due to electrons lost in the image, and background (**Fig. 4**,
242 red curve). We can estimate the average loss of 2DTM SNR, $\overline{SNR_d/SNR_u}$, due to FIB-milling
243 damage from the product of the loss (Eq. (1)) from both surfaces:

$$244$$
$$245 \quad \overline{SNR_d/SNR_u} = \frac{1}{t} \int_0^t \left(1 - e^{-\frac{d}{k}}\right) \cdot \left(1 - e^{-\frac{d-t}{k}}\right) \delta d \quad (3)$$
$$246$$
$$247$$

248 Combining these two sources of signal loss gives the expected overall 2DTM SNR as a function
249 of sample thickness (**Fig. 4**, black curve):

$$250$$
$$251 \quad \overline{SNR_t/SNR_u} = \frac{\left(\int_0^t \left(1 - e^{-\frac{d}{k}}\right) \cdot \left(1 - e^{-\frac{d-t}{k}}\right) \delta d\right) e^{-t/\lambda_{SNR}}}{t} \quad (4)$$
$$252$$

253 This model predicts that in samples thicker than ~ 90 nm, the relative loss in the signal
254 due to the loss of electrons contributing to the image, as well as molecular overlap is greater than
255 the relative change due to FIB-milling damage (**Fig. 4A**). In lamellae thinner than 90 nm,
256 however, FIB-milling damage will dominate and negate any benefit from further thinning. The
257 difference between the expected signal loss given by Eq. (4) and signal loss solely from lost
258 electrons and molecular overlap represents the potential gain if FIB-milling damage could be

259 avoided. Without FIB damage, the potential improvement in 2DTM SNR would be between
260 ~10% in 200 nm lamellae and ~20% in 100 nm lamellae (Fig. 4). The model in Eq. (4) ignores
261 the variable degree of damage expected to occur across LSUs that we used as probes to measure
262 damage, and that have a radius of ~15 nm. However, the resulting error in the measured damage
263 constant k (Eq. (1)) is expected to be small since k (~37 nm) significantly exceeds the LSU
264 radius and hence, the variable damage can be approximated by an average damage uniformly
265 distributed across the target.

266 We also expect that the number of detected targets will be reduced by FIB-milling
267 damage. The number of detected LSUs was variable across lamellae, likely due to biological
268 differences in local ribosome concentration. In undamaged parts of a subset of 200 nm thick
269 lamellae, we identified ~425 LSU in z-coordinate intervals of 10 nm. If this density were
270 maintained throughout the lamella, we would expect to detect ~40% more targets in these
271 lamellae.

272 We conclude that FIB-damage reduces the number and integrity of detected targets but
273 that signal loss due to electrons lost to the image, as well as background from overlapping
274 molecules is a greater limiting factor for target detection and characterization with 2DTM than
275 FIB-milling damage in lamellae thicker than ~90 nm. These data agree with other empirical
276 observations that thinner lamellae are optimal for recovery of structural information and
277 generation of high-resolution reconstructions.

278 It may be possible to restore signal in images otherwise lost to inelastic scattering using
279 Cc-correctors (22). This would be particularly impactful for thick samples such as FIB-milled
280 cellular lamellae. With the use of a Cc-corrector, the signal loss in thick samples would be
281 reduced and FIB-milling damage may become the main limiting factor for *in situ* structural
282 biology.

283

284 **Discussion:**

285

286 Ga⁺ LMIS FIB-milling is currently the preferred method for generating thin, electron-transparent
287 cell sections for *in situ* cryo-EM. We use 2DTM to evaluate the structural integrity of
288 macromolecules in FIB-milled lamellae and provide evidence that FIB-milled lamellae have a
289 region of structural damage to a depth of up to 60 nm from the lamella surface. By evaluating the

290 relative similarity of a target molecule to a template model, 2DTM provides a sensitive, highly
291 position-specific, single particle evaluation of sample integrity.

292

293 ***2DTM SNRs provide a readout of sample integrity and image quality***

294 Changes to the 2DTM SNR provide a read-out of the relative similarity of a target
295 molecule to a given template. We have previously shown that relative 2DTM SNRs discriminate
296 between molecular states and can reveal target identity (17, 18). In this study we show that
297 changes in 2DTM SNRs can also reflect damage introduced during FIB-milling and radiation
298 damage introduced during cryo-EM imaging. Previous attempts to measure FIB-damage have
299 relied on visual changes in the sample near the surface. These changes are difficult to quantify in
300 terms of damage, and they could in part be caused by other mechanisms such as ice
301 accumulation after milling (23). Argon plasma FIB-damage has been assessed by estimating B-
302 factors of subtomogram averages, comparing averages of particles at less than and greater than
303 30 nm from the lamella surface, which lacks positional precision (24). The 2DTM SNR
304 represents a more quantitative metric to assess sample integrity.

305 2DTM SNRs have also been used as a metric to assess image quality (25) and the fidelity
306 of simulations (26). 2DTM therefore, represents a sensitive, quantitative, and versatile method to
307 measure the dependence of data quality on sample preparation and data collection strategies, as
308 well as new hardware technologies and image processing pipelines. Tool and method developers
309 could use standard datasets and 2DTM to rapidly and quantitatively assess how any changes to a
310 pipeline affect data quality.

311

312 ***Estimating errors in z-coordinates and thickness***

313 The z-coordinates of each LSU were determined by modulating the template with a CTF
314 corresponding to a range of defoci and identifying the defocus at which the cross-correlation
315 with the 2D projection image was maximized (15). This quantification relies on an accurate
316 estimate of defocus. The error in the z-coordinates determined this way was estimated to be
317 about 60 Å (17). However, it is unlikely that these errors explain the observed decrease in 2DTM
318 SNRs of LSUs near the edge of the lamellae because (1) the reduction in 2DTM SNRs correlates
319 strongly with the z-coordinate within the lamella, and (2), we did not observe a consistent
320 decrease in the number of detected LSUs (*SI Appendix, Fig. S4A*), or their 2DTM SNRs (*SI*

321 Appendix, **Fig. S4B**) as a function of z-coordinate in images of unmilled *M. pneumoniae* cells
322 (17).

323 Undulations at the lamella surface caused by curtaining or other milling artifacts could
324 contribute to the reduced number of ribosomes detected near the lamella surface. We aimed to
325 minimize the effect of curtaining in our analysis by calculating the lamella thickness in 120 x
326 120 pixel (127.2 x 127.2 Å) patches across an image and limiting our analysis to images with a
327 thickness standard deviation of less than 20 nm. The curtaining on the remaining lamellae cannot
328 account for the reduced particle integrity towards the lamella surface.

329

330 *Possible mechanisms of FIB-milling damage*

331 We find evidence for FIB-milling damage consistent with an exponential decay of the
332 amount of damage as a function of distance from the lamella surface, as measured by the 2DTM
333 SNR. Unlike electron radiation damage, FIB-damage 1) causes a reduction in the total signal and
334 does not preferentially affect higher spatial frequencies contributing to the 2DTM SNR
335 calculation, and 2), unlike electron beam radiation damage, it does not preferentially affect the
336 phosphodiester bond in the RNA backbone. This suggests that different mechanisms are
337 responsible for the damage caused by high-energy electrons and ions.

338 At the energy ranges used for FIB-milling, the interactions between the bombarding ion
339 and sample atoms can be modelled as a cascade of atom displacements resulting from the
340 transfer of momentum from the incident Ga⁺ ions to the sample atoms (13). Atoms involved in
341 the cascade will be displaced while the position of other atoms will not change. This is consistent
342 with our observation that FIB damage decreases the LSU target signal overall without changing
343 the relative contribution from different spatial frequencies. Further study is required to test this
344 hypothesis and investigate the mechanism of FIB-milling damage in more detail.

345 SRIM simulations predict implantation of Ga⁺ up to ~25 nm into the sample (5, 12). This
346 implies that the damage deeper in the sample is caused by secondary effects, possibly reflecting
347 displaced sample atoms that were part of the collision cascade. Interestingly, we observe a
348 different pattern of particles within 20 nm of the lamella surface (**Fig. 3C and D**). One possible
349 explanation is that implanted Ga⁺ ions cause additional damage. However, SRIM simulations
350 have been shown previously not to account for the full intensity profile of a Ga⁺ beam, and
351 poorly match with experiment especially at low beam currents (27). Moreover, the use of a

352 protective organo-platinum layer during FIB-milling, as done in our experiments, will further
353 change the effective profile of the beam acting on the sample (28). Further work is required to
354 connect the quantification of particle integrity with the implantation of Ga⁺ ions during
355 biological lamella preparation.

356

357 *Implications for generating high resolution reconstructions from FIB-milled samples*

358 We have shown that particles on the edge of a lamella have reduced structural integrity
359 relative to particles near the center of the lamella (**Fig. 1 and 2**). We found that FIB-milling
360 damage reduces the total 2DTM SNR and that >20 nm from the lamella surface the rate of signal
361 loss is similar at different spatial frequencies, in contrast to radiation damage during cryo-EM
362 imaging (**Fig. 3**). The practical implication of this finding is that particles >30 nm from the
363 lamella surface can be included during subtomogram averaging without negatively affecting the
364 resolution of the reconstruction, provided they can be accurately aligned. We also predict that
365 more particles will be required relative to unmilled samples. This is consistent with the
366 observation that more particles <30 nm from the lamella surface are required to achieve the same
367 resolution relative to >30 nm from the lamella surface from Argon plasma FIB-milled lamellae
368 (24).

369 Due to the small number of particles detected within 10 nm of the lamella surface, these
370 particles were not examined in more detail. Since ribosomes are ~25 nm in diameter, it is likely
371 that these particles are more severely damaged compared to particles further away from the
372 surface. 2DTM relies on high-resolution signal and therefore excludes more severely damaged
373 particles that may be included using a low-resolution template matching approach, such as 3D
374 template matching used typically to identify particles for subtomogram averaging. We therefore
375 advise excluding particles detected within 10 nm of the lamella surface.

376

377 *Alternate methods for the preparation of thin cell sections*

378 FIB damage reduces both the number of detected targets and the available signal per target.
379 However, the damaged volume still contributes to the sample thickness, reducing the usable
380 signal by 10-20% in lamellae of typical thicknesses (**Fig. 4**). Therefore, it would be
381 advantageous to explore other strategies for cell thinning.

382 Plasma FIBs allow different ions to be used for milling, and this may change the damage
383 profile (29). Larger atoms such as Xenon will have a higher sputtering yield and may result in
384 reduced lamella damage, as has been demonstrated for milling of silicon samples (30, 31). The
385 2DTM-based approach described here provides a straightforward way to quantify the relative
386 damaging effects of different ion species by generating curves as shown in Fig. 4.

387 CEMOVIS generates thin sections using a diamond knife rather than high energy ions
388 and would therefore not introduce radiation damage (2). It is unclear how the large-scale
389 compression artifacts introduced by this method affect particle integrity (3). CEMOVIS has the
390 additional benefit of being able to generate multiple sections per cell and thereby enable serial
391 imaging of larger cell volumes. If the compression artifacts are unevenly distributed throughout a
392 section, leaving some regions undistorted, automation could make CEMOVIS a viable strategy
393 for structural cell biology in the future.

394 To retain the benefits of fast, reliable, high-throughput lamella generation with cryo-FIB
395 milling, strategies to remove the damaged layer should be explored. Possibilities include
396 polishing the final ~50 nm from each lamella surface with a low energy (~5 kV) beam, which
397 has the advantage of being easily implementable using the current configuration of most cryo-
398 FIB-SEMs.

399

400 **Materials and Methods**

401 **Yeast culture and Freezing**

402 *Saccharomyces cerevisiae* strains BY4741 (ATCC) colonies were inoculated in 20 mL of
403 YPD, diluted 1/5 and grown overnight at 30 °C with shaking to mid log phase. The cells were
404 then diluted to 10,000 cells/mL, treated with 10 µg/mL cycloheximide (Sigma) for 10 mins at 30
405 °C with shaking and 3 µL applied to a 2/1 or 2/2 Quantifoil 200 mesh SiO₂ Cu grid, allowed to
406 rest for 15 s, back-side blotted for 8 s at 27 °C, 95% humidity followed by plunge freezing in
407 liquid ethane at -184 °C using a Leica EM GP2 plunger. Frozen grids were stored in liquid
408 nitrogen until FIB-milled.

409

410 **FIB-milling**

411 Grids were transferred to an Aquilos 2 cryo-FIB/SEM, sputter coated with metallic Pt for
412 10 s then coated with organo-Pt for 30 s and milled in a series of sequential milling steps using a

413 30kV Ga⁺ LMIS beam using the following protocol: rough milling 1: 0.1 nA rough milling 2: 50
414 pA lamella polishing: 10 pA at a stage tilt of 15° (milling angle of 8°) or 18° (milling angle of
415 11°).

416

417 **Cryo-EM data collection and image processing**

418 Cryo-EM data was collected following the protocol described in (18) using a Thermo
419 Fisher Krios 300 kV electron microscope equipped with a Gatan K3 direct detector and Gatan
420 energy filter with a slit width of 20 eV at a nominal magnification of 81,000x (pixel size of 1.06
421 Å²) and a 100 μm objective aperture. Movies were collected at an exposure rate of 1 e⁻/Å²/frame
422 to a total dose of 50 e⁻/Å² (Dataset 1) or 30 e⁻/Å² (Dataset 2) with correlated double sampling
423 using the microscope control software SerialEM (32).

424 Images were processed as described previously (18). Briefly, movie frames were aligned
425 using the program *unblur* (33) in the *cisTEM* GUI (34) with or without dose weighting using the
426 default parameters where indicated in the text. Defocus, astigmatism, and sample tilt were
427 estimated using a modified version of CTFFIND4 (17, 19) in the *cisTEM* GUI (34). Images of
428 cytoplasm were identified visually for further analysis. Images visually containing organelles
429 were excluded. Images of 3D densities and 2DTM results were prepared in ChimeraX (35).

430

431 **2DTM**

432 The atomic coordinates corresponding to the yeast LSU from PDB: 6Q8Y (36) were used
433 to generate a 3D volume using the *cisTEM* program *simulate* (26) and custom scripts as in (21).
434 2DTM was performed using the program *match_template* (20) in the *cisTEM* GUI (34) using an
435 in-plane search step of 1.5° and an out-of-plane search step of 2.5°. Significant targets were
436 defined as described in (15) and based on the significance criterion described in (16). The
437 coordinates were refined using the program *refine_template* (18) in rotational steps of 0.1° and a
438 defocus range of 200 Å with a 20 Å step (2 nm z-precision). The template volume was placed in
439 the identified locations and orientations using the program *make_template_result* (17) and
440 visualized with ChimeraX (35).

441 To generate the results in Fig. 3A-D, we applied a series of sharp low-pass filters in steps
442 of 0.01 Å⁻¹ to the template using the *e2proc3d.py* function in EMAN2 (37). We used the
443 locations and orientations from the refined 2DTM search with the full-length template to

444 recalculate the 2DTM SNR with each modified template using the program *refine_template* (18)
445 by keeping the positions and orientations fixed. The normalized cross-correlation was
446 determined by dividing the SNR calculated with each low-pass filtered template to the SNR of
447 the full-length template for each target.

448

449 **Calculation of tilt and coordinate transform**

450 We used python scripts to extract the rotation angle and tilt from the *cisTEM* (34)
451 database generated using the tilt-enabled version of the program CTFFIND4 (18, 19), perform a
452 coordinate transform to convert the 2DTM coordinates to the lamella coordinate frame and plot
453 the 2DTM SNR as a function of lamella z-coordinate.

454

455 **Calculation of sample thickness and depth**

456 We estimated the lamella thickness per image by first summing the movie frames without
457 dose weighting using the EMAN2 program, *alignframes* (37), then calculating the average
458 intensity of a sliding box of 100 x 100 pixels (I) relative to the same area of an image collected
459 over vacuum (I_o). We then used the mean free path for electron scattering (λ) of 283 nm (16) to
460 estimate the local sample thickness t_i using the Beer-Lambert law (38):

461

$$462 \quad t_i = -\ln\left(\frac{I}{I_o}\right)\lambda \quad (5)$$

463

464 The sample thickness was determined by taking the mean across the image. Only images with a
465 standard deviation of <20 nm across the image were included for estimation of the damage
466 profile (**Fig. 2B**). The depth of each LSU relative to the lamella surface was calculated by
467 assuming that the LSUs are evenly distributed in z and defining the median lamella z coordinate
468 as the lamella center (e.g.: **Fig. 1G,H and S2**).

469

470 **Measuring change in signal with electron exposure**

471 We compared the change in the 2DTM SNR of each individual LSU as a function of
472 electron exposure at different positions relative to the edge of the lamella in bins of 10 nm. We
473 used the locations and orientations of LSUs identified in dose-filtered images exposed to $50 \text{ e}^-/\text{\AA}^2$

474 to assess the correlation at the same locations and orientations in different numbers of
475 unweighted frames corresponding to total exposures of 8-36 e⁻/Å².

476 To calculate the relative contribution of phosphorous to the 2DTM SNR all phosphorous
477 atoms in the PDB file were deleted and a template was generated as described above without re-
478 centering so that it aligned with the full-length template. We used the locations and orientations
479 from the refined 2DTM search with the full-length template for each exposure to calculate the
480 2DTM SNR with the template lacking phosphorous ($SNR_{\Delta P}$) using the program *refine_template*
481 (18) and keeping the positions and orientations fixed. The relative contribution of phosphorous
482 atoms to the 2DTM SNR (SNR_P) at each exposure was calculated using the following equation:

$$483 \quad SNR_P = 1 - \frac{SNR_{\Delta P}}{SNR_{FL}} \quad (6)$$

484

485 **Acknowledgements:**

486 The authors thank Johannes Elferich, Ximena Zottig and other members of the Grigorieff lab
487 (UMass Chan), Russo lab (MRC LMB) and de Marco lab (Monash) for helpful discussions. We
488 are also grateful for the use of and support from the cryo-EM facilities at Janelia Research
489 Campus and UMass Chan Medical School.

490

491 **Funding:**

492 BAL and NG gratefully acknowledge funding from the Chan Zuckerberg Initiative, grant #
493 2021-234617 (5022).

494 **Figure Legends:**

495

496 **Figure 1: Visualization of yeast cytoplasmic ribosomes in 3D with 2DTM.** (A) An electron
497 micrograph of the yeast cytoplasm in a 120 nm region of a lamella. Scale bars in A) and B)
498 represent 50 nm. (B) As in A), showing a 200 nm lamella. (C) Significant large ribosomal
499 subunits (LSUs) located in 3D in the image in A) with 2DTM. (D) As in C), showing the results
500 for the image in B). (E) Scatterplot showing a side view of the LSUs in A). The color coding
501 indicates the 2DTM SNR of each significant detection relative to the mean 2DTM SNR. The z-
502 coordinate represents the position of each target relative to the microscope defocus plane. (F) As
503 in E), showing the results from the image in B). (G) Scatterplot showing the 2DTM SNR of each
504 detected LSU in the image in A), as a function of z-coordinate relative to the lamella. (H) As in
505 G), showing the z-coordinate relative to the center of the lamella of each LSU detected in the
506 image shown in B).

507

508 **Figure 2: The number and 2DTM SNR values of detected LSUs increases as a function of**
509 **distance from the lamella surface.** (A) Boxplot showing the 2DTM SNR of LSUs at the
510 indicated lamella depths, relative to the undamaged SNR (SNR_u) in each image from 200 nm
511 lamellae. Boxes represent the interquartile range (IQR), middle line indicates the median,
512 whiskers represent 1.5x IQR and dots represent values outside of this range. (B) Scatterplot
513 showing the number of detected targets in the indicated z-coordinate bins. (C) Gaussian fits to
514 the distribution of 2DTM SNRs for LSUs identified in z-coordinate bins of 10 nm. Red indicates
515 populations with means significantly different from the mean in the center of the lamella. Blue
516 indicates that the mean in a bin is not significantly different from the mean in the center. Fitting
517 statistics are indicated in *SI Appendix, Table S1*. (D) Scatterplot showing the mean change in
518 2DTM SNR relative to SNR_u at the indicated depths relative to the lamella surface estimated
519 from the Gaussian fits in C). The line shows the exponential fit ($R^2 = 0.99$). Error bars indicated
520 the standard deviation from the Gaussian fit.

521

522 **Figure 3: The mechanism of FIB-milling damage is distinct from radiation damage during**
523 **cryo-EM imaging.** (A) Plot showing the change in 2DTM SNR with the template low-pass
524 filtered to the indicated spatial frequency in images collected with the indicated number of

525 electrons/ \AA^2 relative to the same filtered template with 20 electrons/ \AA^2 . **(B)** Plot showing the
526 change in 2DTM SNR as a function of electron exposure of templates low-pass filtered to the
527 indicated spatial frequency. **(C)** As in A), showing the change in the 2DTM SNR in the indicated
528 lamella z-coordinate bins relative to the SNR in the undamaged bin (SNR_u). **(D)** Plot showing
529 the change in 2DTM SNR for templates low-pass filtered to the indicated spatial frequencies as a
530 function of lamella z-coordinate bins. **(E)** Diagram showing a segment of an RNA strand of two
531 nucleotides. The blue circle designates the phosphate; the two red arrows indicate the location of
532 the backbone phosphodiester bonds. **(F)** Plot showing the relative contribution of template
533 phosphorous atoms to the 2DTM SNR relative to the full-length template at the indicated
534 exposure without dose weighting calculated using equation (6).

535

536 **Figure 4: Signal loss due to increased electron scattering in thicker samples outweighs the**
537 **effect of FIB damage on LSU 2DTM SNRs.** Plot showing the expected signal recovery in
538 lamellae of indicated thickness as a function of signal loss due to electron scattering (red curve),
539 FIB-damage (blue curve) and their product (black curve).

540

541 **Figure S1: (A)** Histogram showing the distribution of lamella thickness calculated using the
542 Beer-Lambert law. **(B)** Scatterplot showing the mean 2DTM SNR of the detected LSUs in each
543 image as a function of local lamella thickness. The point size indicates the number of LSUs
544 detected in the image.

545

546 **Figure S2:** Representative plots showing the relationship between lamella z-coordinate and
547 2DTM SNR of LSU-detected targets in FIB-milled yeast lamellae.

548

549 **Figure S3:** Scatterplot showing the mean number of targets detected in each lamella z-
550 coordinate bin for lamellae of the indicated thickness. Error bars indicate the standard deviation

551

552 **Figure S4: No consistent relationship between 2DTM SNRs and depth in unmilled**
553 ***Mycoplasma pneumoniae* cells.** **(A)** Scatterplot showing the mean proportion of LSUs identified
554 in each bin as a function of distance from the edge of the ribosome occupied volume (ROV). **(B)**
555 Scatterplot showing the 2DTM SNR relative to the image mean for each identified LSU as a

556 function of distance from the edge of the ROV. **(C)** Plot showing the z-dimension of the ROV in
557 images of *Mycoplasma pneumoniae* cells. **(D)** As in A), showing the results grouped by
558 thickness.

559

560 **Figure S5:** Scatterplots showing the 2DTM SNRs of LSU-detected targets in images of unmilled
561 *Mycoplasma pneumoniae* cells as a function of z-coordinate relative to the defocus plane at x =
562 0.

563

564

- 565 1. W. Baumeister, R. Grimm, J. Walz, Electron tomography of molecules and cells. *Trends*
566 *Cell Biol* **9**, 81–85 (1999).
- 567 2. A. Al-Amoudi, L. P. O. Norlen, J. Dubochet, Cryo-electron microscopy of vitreous sections
568 of native biological cells and tissues. *J Struct Biol* **148**, 131–135 (2004).
- 569 3. A. Al-Amoudi, D. Studer, J. Dubochet, Cutting artefacts and cutting process in vitreous
570 sections for cryo-electron microscopy. *J Struct Biol* **150**, 109–121 (2005).
- 571 4. M. Marko, C. Hsieh, W. Moberlychan, C. A. Mannella, J. Frank, Focused ion beam milling
572 of vitreous water: Prospects for an alternative to cryo-ultramicrotomy of frozen-hydrated
573 biological samples. *J Microsc* **222**, 42–7 (2006).
- 574 5. M. Marko, C. Hsieh, R. Schalek, J. Frank, C. Mannella, Focused-ion-beam thinning of
575 frozen-hydrated biological specimens for cryo-electron microscopy. *Nature Methods*
576 *2007* **4**:3 **4**, 215–217 (2007).
- 577 6. A. Rigort, *et al.*, Focused ion beam micromachining of eukaryotic cells for cryoelectron
578 tomography. *Proc Natl Acad Sci U S A* **109**, 4449–4454 (2012).
- 579 7. G. Buckley, *et al.*, Automated cryo-lamella preparation for high-throughput in-situ
580 structural biology. *J Struct Biol* **210**, 107488 (2020).
- 581 8. T. Zachs, *et al.*, Fully automated, sequential focused ion beam milling for cryo-electron
582 tomography. *Elife* **9** (2020).
- 583 9. M. Schaffer, *et al.*, Cryo-FIB Lamella Milling: A Comprehensive Technique to Prepare
584 Samples of Both Plunge- and High-pressure Frozen-hydrated Specimens for in situ
585 Studies. *Microscopy and Microanalysis* **24**, 820–821 (2018).
- 586 10. D. Tegunov, L. Xue, C. Dienemann, P. Cramer, J. Mahamid, Multi-particle cryo-EM
587 refinement with M visualizes ribosome-antibiotic complex at 3.5 Å in cells. *Nat Methods*
588 **18**, 186–193 (2021).
- 589 11. B. A. Himes, P. Zhang, emClarity: software for high-resolution cryo-electron tomography
590 and subtomogram averaging. *Nat Methods* **15**, 955–961 (2018).
- 591 12. Y. Fukuda, A. Leis, A. Rigort, Preparation of Vitrified Cells for TEM by Cryo-FIB
592 Microscopy. *Biological Field Emission Scanning Electron Microscopy: Volume I: Volume II*
593 **1–2**, 415–438 (2019).
- 594 13. L. A. Giannuzzi, B. I. Prenitzer, B. W. Kempshall, Ion - Solid Interactions. *Introduction to*
595 *Focused Ion Beams*, 13–52 (2005).
- 596 14. J. L. Vilas, *et al.*, Measurement of local resolution in electron tomography. *J Struct Biol X*
597 **4**, 100016 (2020).
- 598 15. J. P. Rickgauer, N. Grigorieff, W. Denk, Single-protein detection in crowded molecular
599 environments in cryo-EM images. *Elife* **6**, e25648 (2017).
- 600 16. J. P. Rickgauer, H. Choi, J. Lippincott-Schwartz, W. Denk, Label-free single-instance
601 protein detection in vitrified cells. *bioRxiv*, 2020.04.22.053868 (2020).
- 602 17. B. A. Lucas, *et al.*, Locating macromolecular assemblies in cells by 2D template matching
603 with cisTEM. *Elife* **10** (2021).
- 604 18. B. A. Lucas, K. Zhang, S. Loerch, N. Grigorieff, In situ single particle classification reveals
605 distinct 60S maturation intermediates in cells. *Elife* **11** (2022).
- 606 19. A. Rohou, N. Grigorieff, CTFFIND4: Fast and accurate defocus estimation from electron
607 micrographs. *J Struct Biol* **192**, 216–221 (2015).

- 608 20. L. A. Baker, J. L. Rubinstein, Radiation damage in electron cryomicroscopy. *Methods*
609 *Enzymol* **481**, 371–388 (2010).
- 610 21. J. F. Ward, Molecular Mechanisms of Radiation-Induced Damage to Nucleic Acids. **5**,
611 181–239 (1975).
- 612 22. J. L. Dickerson, C. J. Russo, Phase contrast imaging with inelastically scattered electrons
613 from any layer of a thick specimen. *Ultramicroscopy* **237**, 113511 (2022).
- 614 23. C. J. Russo, J. L. Dickerson, K. Naydenova, Cryomicroscopy in situ : what is the smallest
615 molecule that can be directly identified without labels in a cell? *Faraday Discuss* **240**,
616 277–302 (2022).
- 617 24. C. Berger, *et al.*, Plasma FIB milling for the determination of structures in situ. *bioRxiv*,
618 2022.08.01.502333 (2022).
- 619 25. J. Elferich, G. Schioli, D. T. Scadden, N. Grigorieff, Defocus Corrected Large Area Cryo-EM
620 (DeCo-LACE) for label-free detection of molecules across entire cell sections. *Elife* **11**
621 (2022).
- 622 26. B. Himes, N. Grigorieff, Cryo-TEM simulations of amorphous radiation-sensitive samples
623 using multislice wave propagation. *IUCrJ* **8**, 943–953 (2021).
- 624 27. Y. Greenzweig, Y. Drezner, S. Tan, R. H. Livengood, A. Raveh, Current density profile
625 characterization and analysis method for focused ion beam. *Microelectron Eng* **155**, 19–
626 24 (2016).
- 627 28. M. Schaffer, *et al.*, Optimized cryo-focused ion beam sample preparation aimed at in situ
628 structural studies of membrane proteins. *J Struct Biol* **197**, 73–82 (2017).
- 629 29. G. Sergey, *et al.*, Oxygen plasma focused ion beam scanning electron microscopy for
630 biological samples. *bioRxiv*, 457820 (2018).
- 631 30. L. A. Giannuzzi, N. S. Smith, TEM Specimen Preparation with Plasma FIB Xe + Ions.
632 *Microsc. Microanal* **17**, 646–647 (2017).
- 633 31. R. Kelley, *et al.*, Xe + FIB Milling and Measurement of Amorphous Silicon Damage.
634 *Microsc. Microanal* **19**, 862–863 (2013).
- 635 32. D. N. Mastronarde, Automated electron microscope tomography using robust prediction
636 of specimen movements. *J Struct Biol* **152**, 36–51 (2005).
- 637 33. T. Grant, N. Grigorieff, Measuring the optimal exposure for single particle cryo-EM using
638 a 2.6 Å reconstruction of rotavirus VP6. *Elife* **4**, e06980 (2015).
- 639 34. T. Grant, A. Rohou, N. Grigorieff, CisTEM, user-friendly software for single-particle image
640 processing. *Elife* **7**, e35383 (2018).
- 641 35. E. F. Pettersen, *et al.*, UCSF ChimeraX: Structure visualization for researchers, educators,
642 and developers. *Protein Sci* **30**, 70 (2021).
- 643 36. P. Tesina, *et al.*, Structure of the 80S ribosome–Xrn1 nuclease complex. *Nat Struct Mol*
644 *Biol* **26**, 275–280 (2019).
- 645 37. G. Tang, *et al.*, EMAN2: An extensible image processing suite for electron microscopy. *J*
646 *Struct Biol* **157**, 38–46 (2007).
- 647 38. W. J. Rice, *et al.*, Routine Determination of Ice Thickness for Cryo-EM Grids. *J Struct Biol*
648 **204**, 38 (2018).
- 649

Table S1: Gaussian fits to z-coordinate bins in Figure 2

Depth (nm)	Mean	SD	R squared	N	t-test vs 100 nm
10	0.8664	0.09367	0.8148	27	P<0.0001
20	0.8353	0.09015	0.9243	44	P<0.0001
30	0.8733	0.1089	0.9591	161	P<0.0001
40	0.9084	0.115	0.9345	245	P<0.0001
50	0.9405	0.1167	0.989	383	P<0.0001
60	0.9612	0.1193	0.9839	424	P<0.0001
70	0.9859	0.1163	0.9644	421	ns
80	0.9926	0.1207	0.9703	427	ns
90	0.9837	0.1065	0.9676	450	ns
100	1.003	0.1079	0.9865	401	_

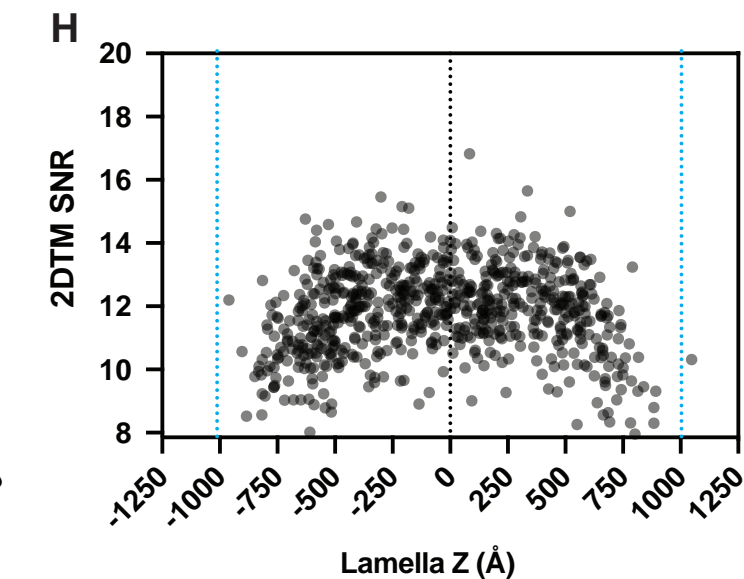
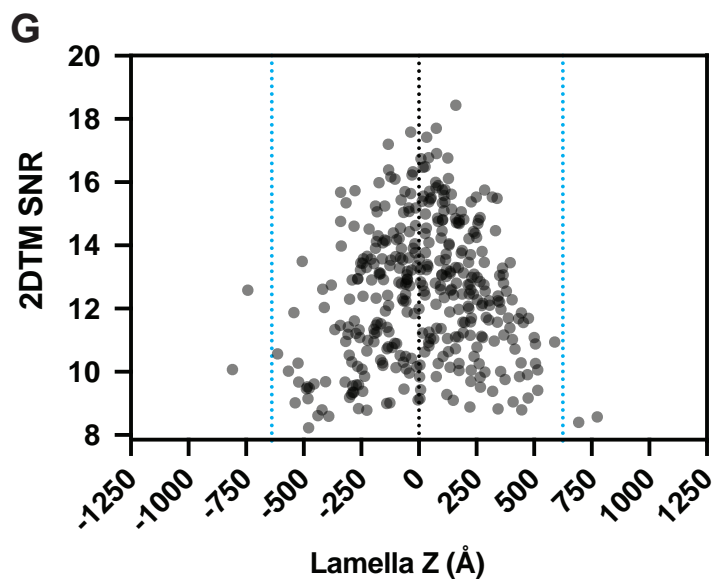
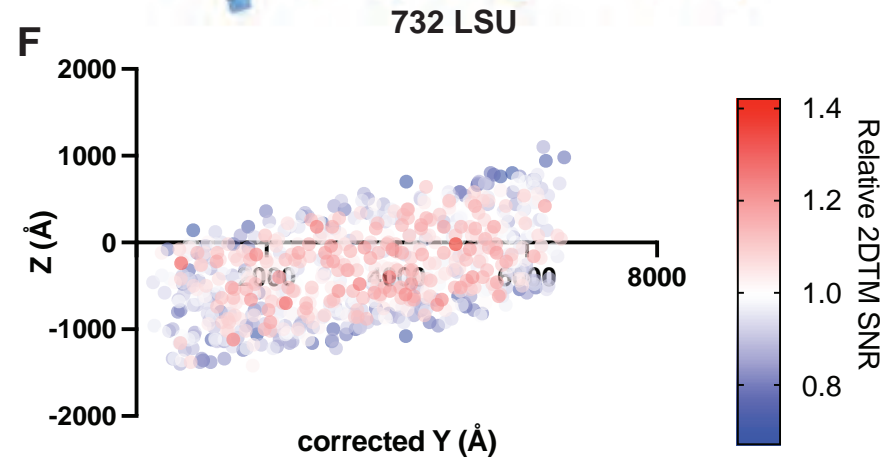
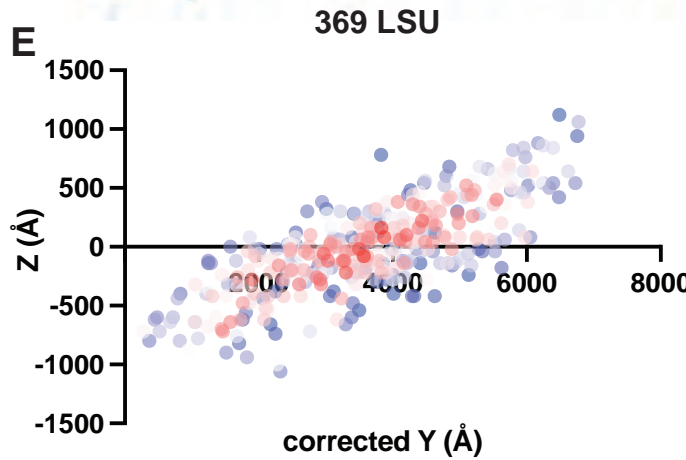
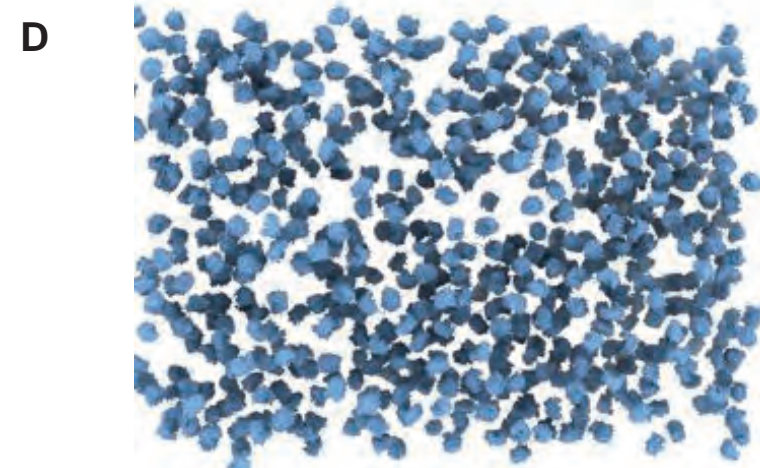
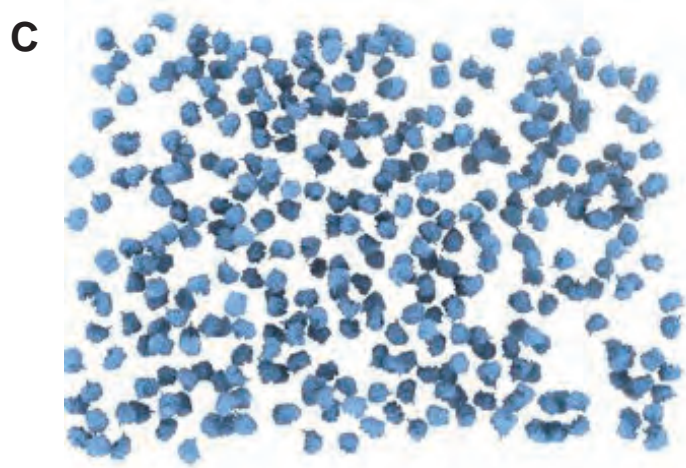
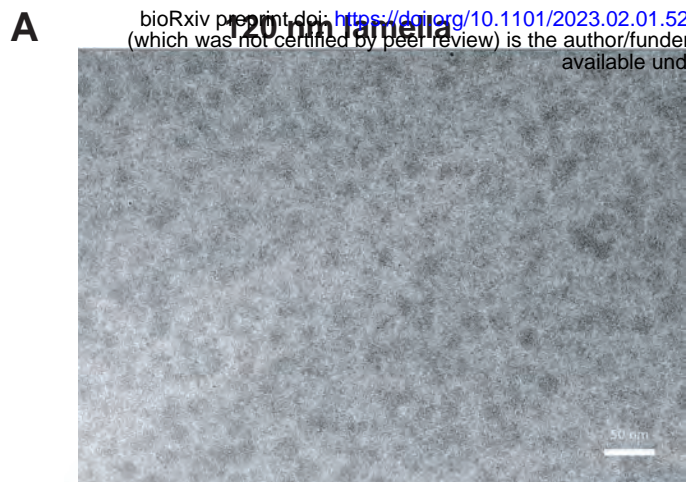
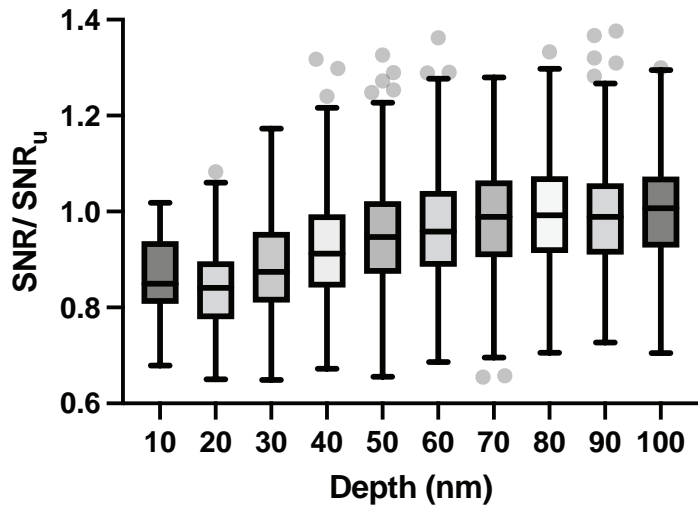
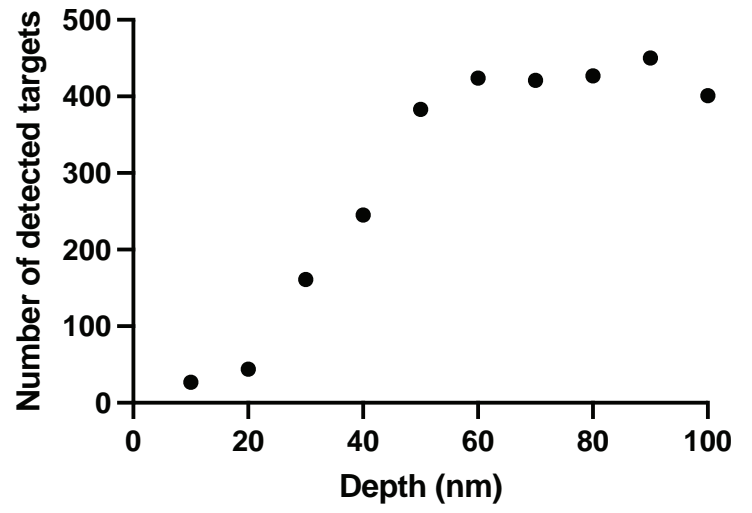


Figure 1

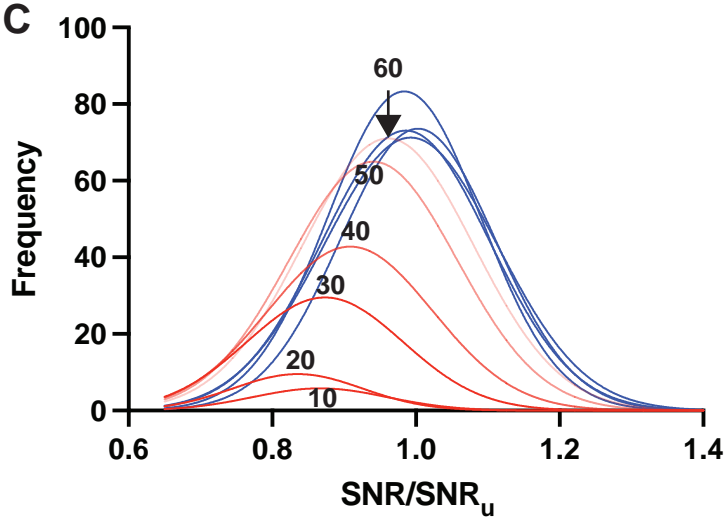
A



B



C



D

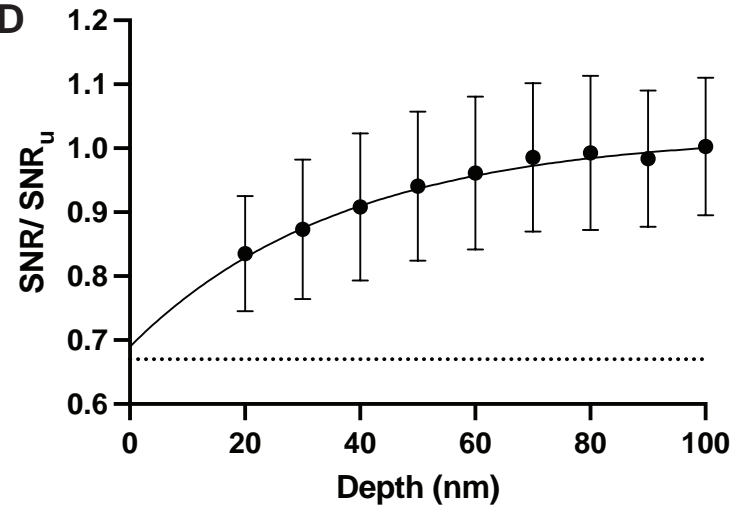


Figure 2

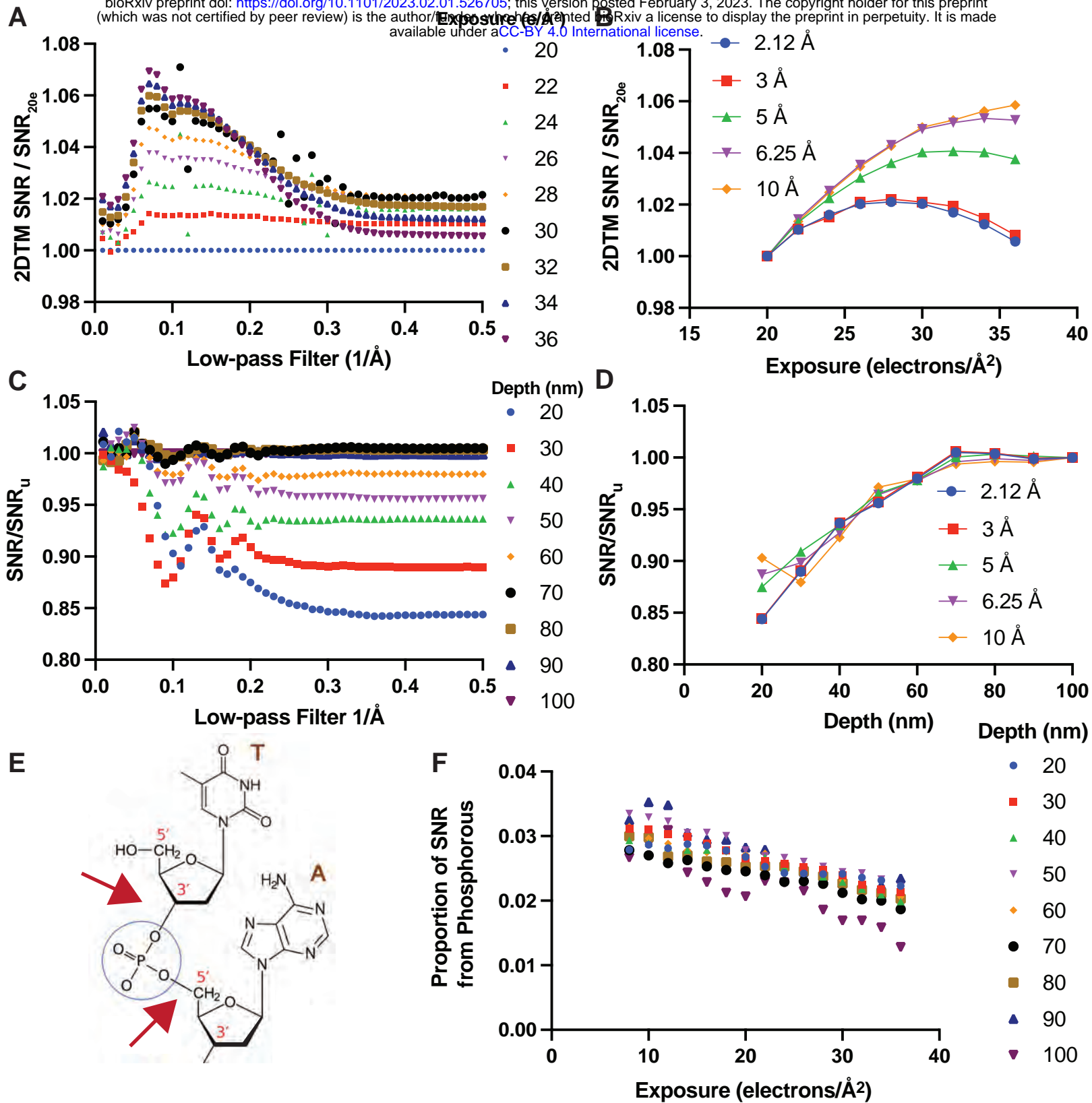


Figure 3

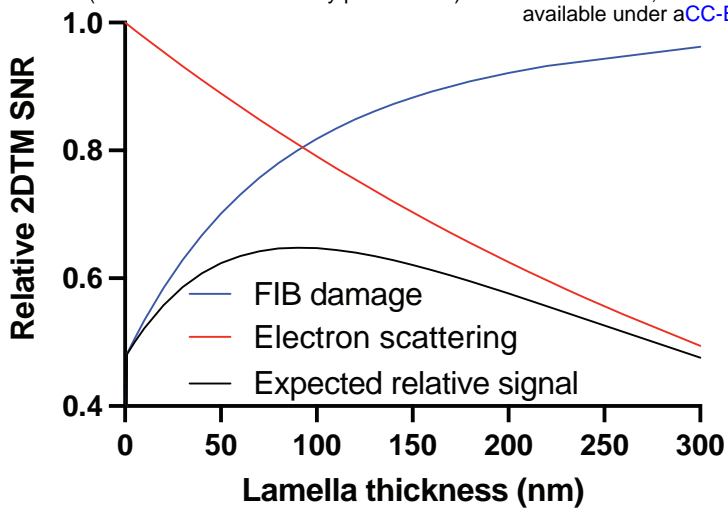
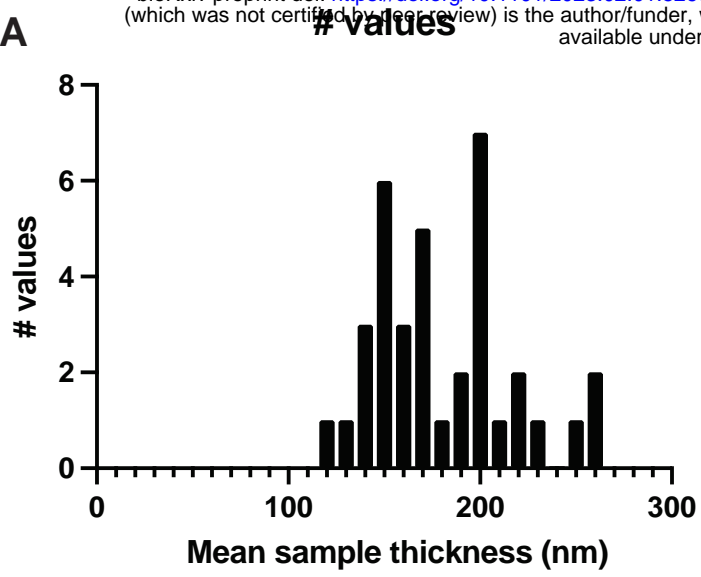


Figure 4

A



B

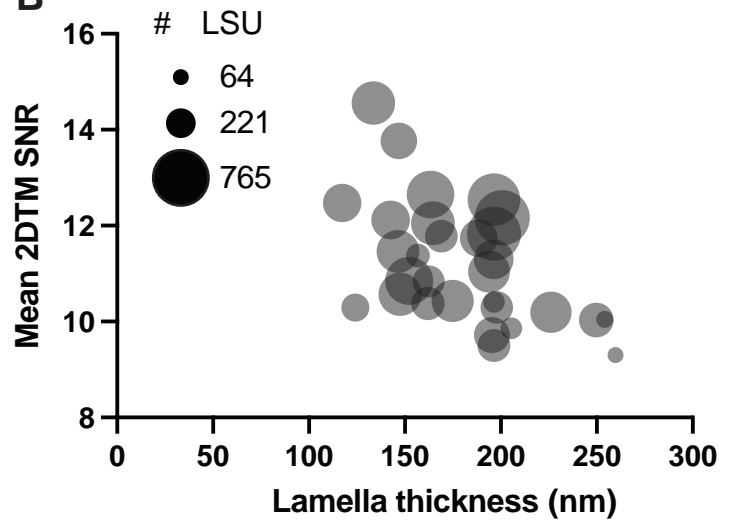


Figure S1

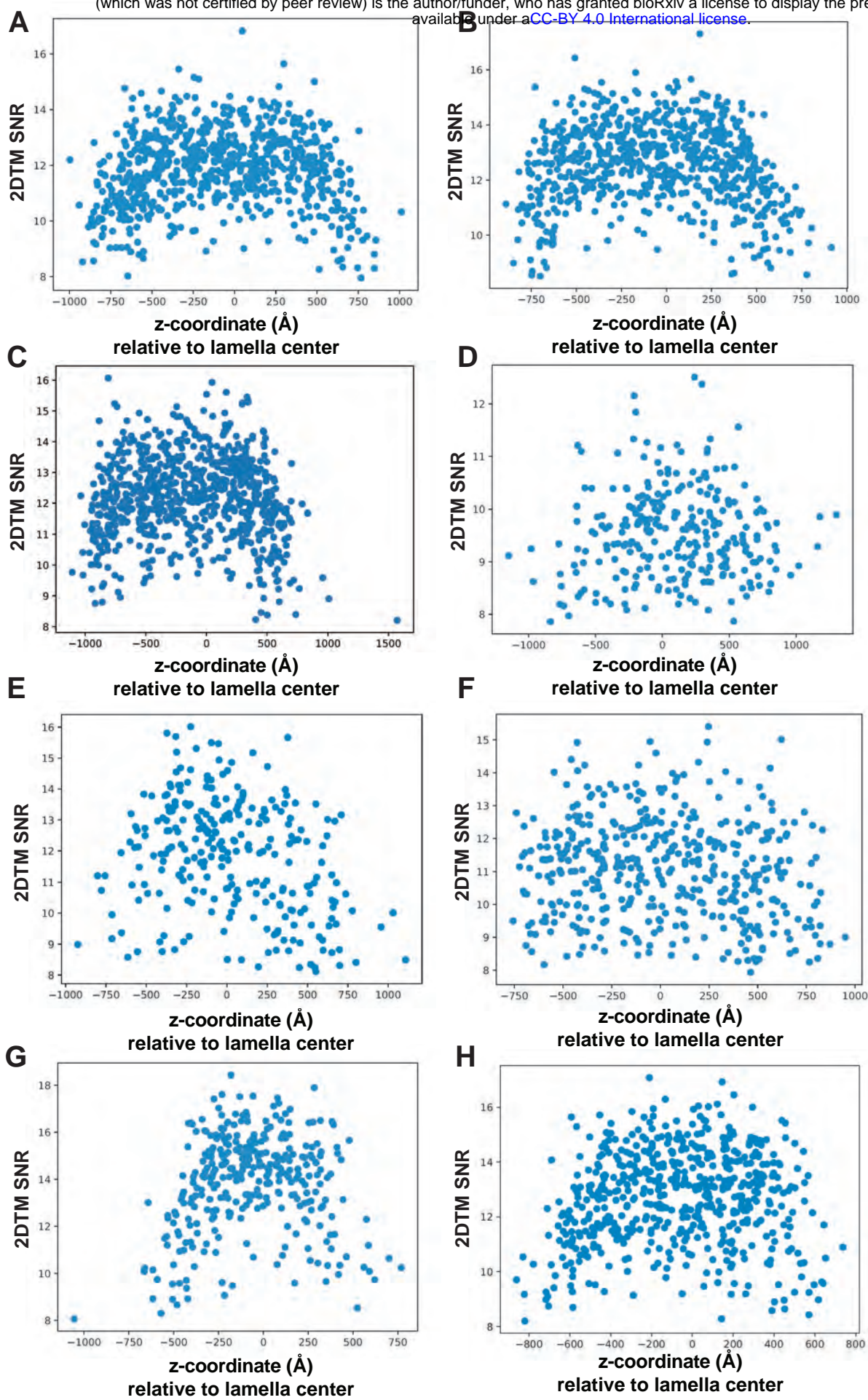


Figure S2

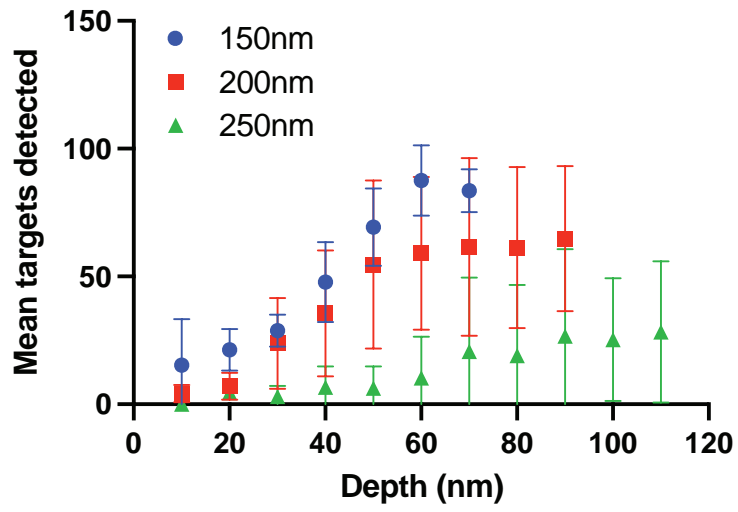


Figure S3

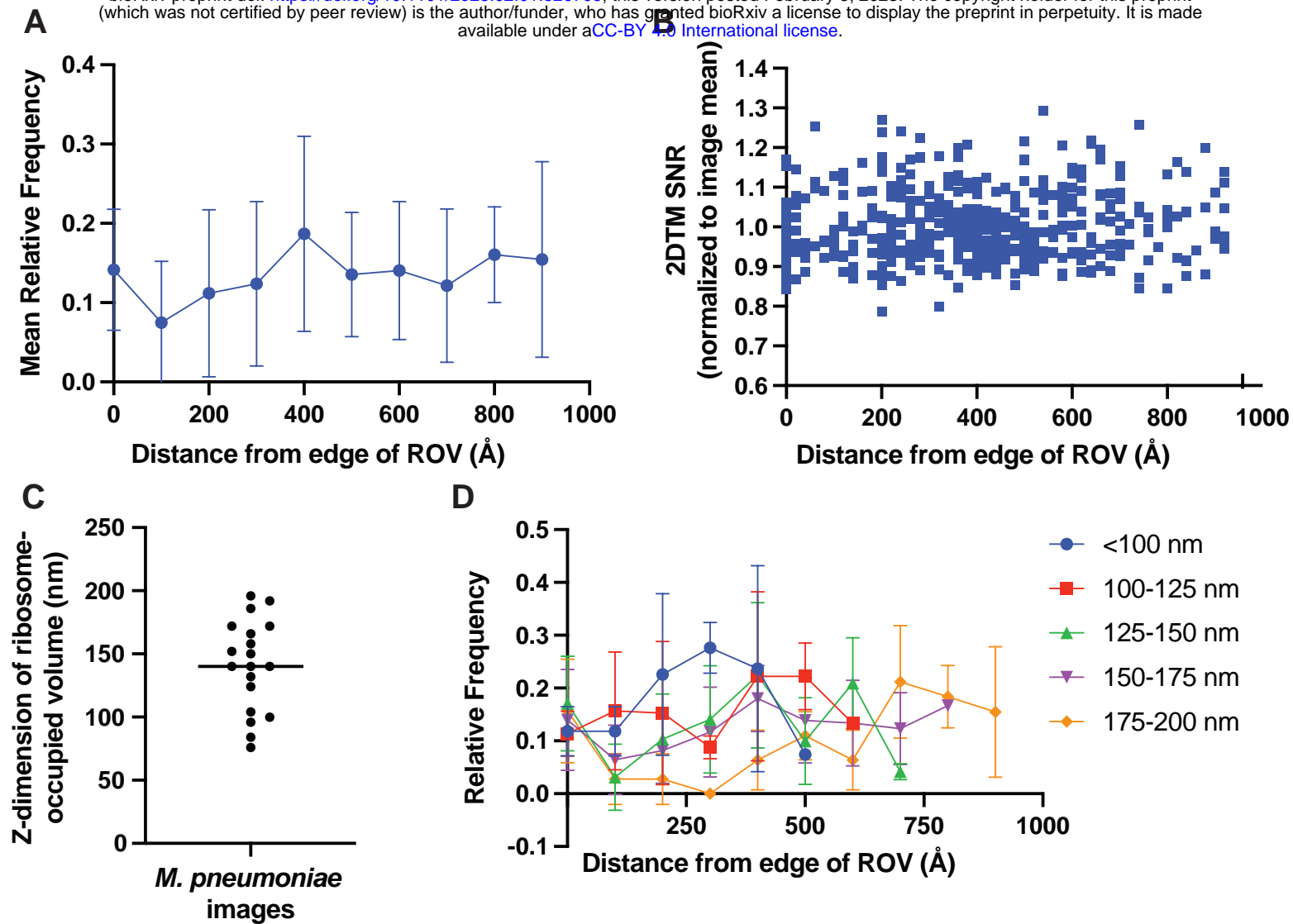


Figure S4

M. pneumoniae unmilled samples

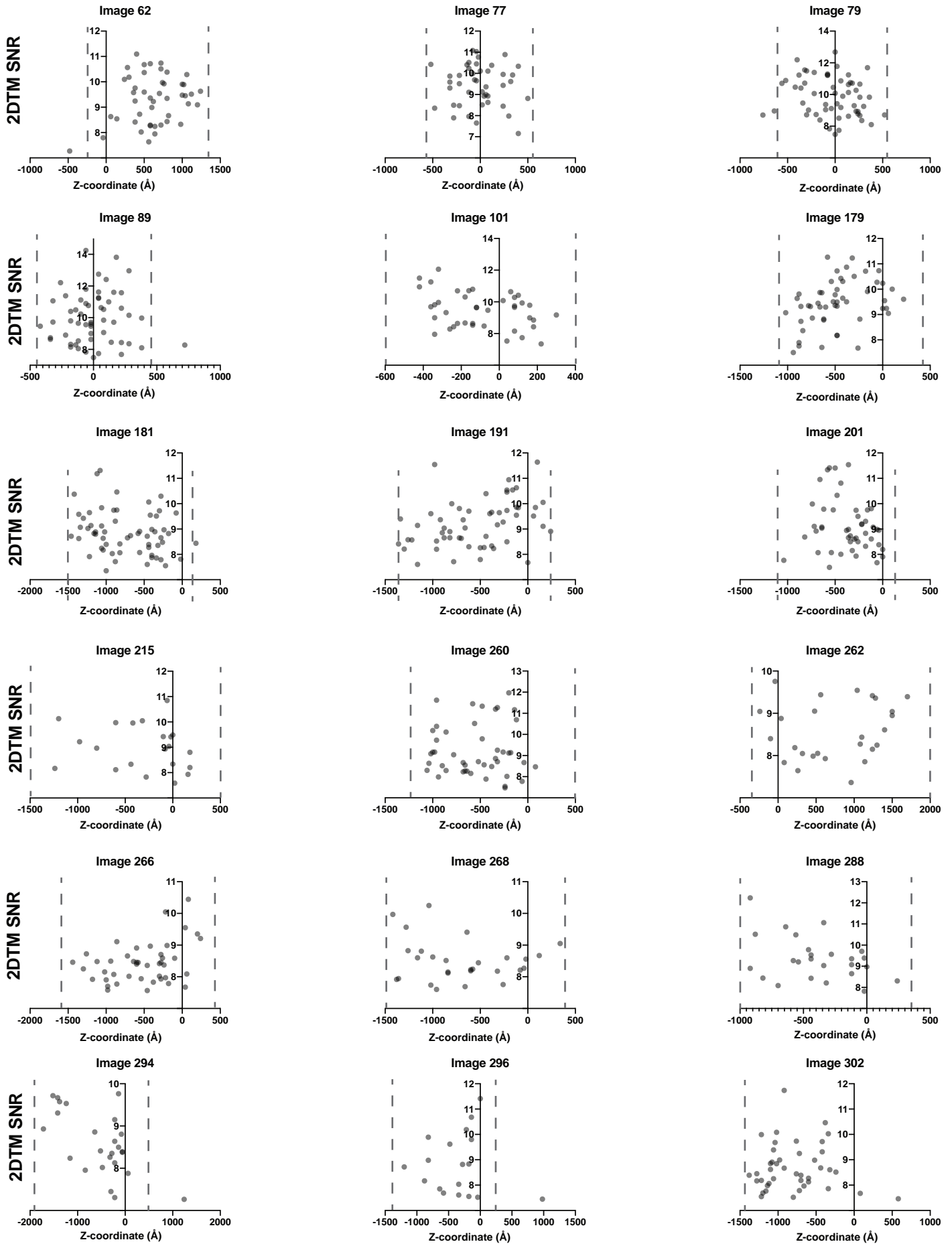


Figure S5